

Triclinic ZnMoO₄ catalyst for atmospheric pressure non-thermal pulsating corona plasma degradation of reactive dye; role of the catalyst in plasma degradation process

Milica Petrović^{1*}, Saša Rančev², Nena Velinov¹, Miljana Radović Vučić¹, Milan Antonijević³, Goran Nikolić⁴, Aleksandar Bojić¹

¹ *University of Niš, Faculty of Science and Mathematics, Department of Chemistry, Višegradaska 33, 18000, Niš, Serbia*

² *University of Niš, Faculty of Science and Mathematics, Department of Physics, Višegaradska 33, 18000, Niš, Serbia*

³ *School of Science, Faculty of Engineering and Science, University of Greenwich at Medway, Central Avenue, Chatham Maritime, Kent, ME4 4TB, England, UK*

⁴ *University of Niš, Faculty of Technology, 124 Bulevar Oslobođenja str., 16000 Leskovac, Serbia*

Abstract

Microcrystalline α -ZnMoO₄ catalyst for degradation of Reactive Black 5 by self-made open air atmospheric pressure pulsating corona plasma reactor was synthesized by electrodeposition, followed by thermal treatment. The effect of electrodeposition current density on the catalyst' characteristics was examined by SEM, EDX, FTIR XRD and TG. The catalyst enhanced plasma decolourization rate by 7.5 times. The role of the catalyst in the consumption of plasma generated H₂O₂ and in dye degradation was examined in details for the first time to the best of our knowledge;

* milicabor84@gmail.com

the catalyst enhanced the generation of $\cdot\text{OH}$ radical, a principle dye degradation reagent, by enhancing decomposition of plasma-generated H_2O_2 . The catalyst' excitation mostly proceeded by the strikes of plasma-generated active species accelerated by electric field, which transferred their energy to the catalyst, causing the creation of electron – holes pairs which attacked H_2O_2 . Decolourization followed pseudo – first order kinetics. Decolourization rate increases with the increase of discharge current density and reactor input voltage. The ratio between cylindrical reactor cell's diameter and the liquid level in it didn't affect the decolourization rate. Relatively high energy yield of 1.86 gkWh^{-1} was achieved for 50% decolourization. TOC removal was 85.4% after 180 minutes of the treatment.

Keywords: catalyst; plasma corona; organics; degradation; mechanism

1.Introduction

Synthetic dyes are present in many industries' wastewaters. They are difficult to remove by conventional physico-chemical processes due to high stability of their molecules, thus, certain alternative processes have been developed, like advance oxidation processes (AOPs). AOPs are based on oxidation of organics by strong short living, non-selective oxidants, like hydroxyl radical, $\cdot\text{OH}$, which causes oxidative degradation of initial compound into smaller fragments, and may lead to complete mineralization. Generation of strong oxidants is caused by some source of energy, like UV radiation etc. Plasma in contact with water can generate reactive ion and radical species, including $\cdot\text{OH}$, electrons and UV radiation, which all can contribute to degradation of organic molecules present in that water. When certain semiconducting materials absorb the energy higher than their band gap, they create electron (e^-) - hole

(h^+) pairs, which can react with H_2O and H_2O_2 , and thus produce reactive species and act like a catalysts (Chandana et al., 2015; García et al., 2017; Wang et al., 2018; Wang et al., 2017; Mahmoodi et al., 2018). Recently, application of various types of plasma in degradation of organics was investigated (Chandana et al., 2015; Wang et al., 2018; Magureanu et al., 2015; Jiang et al., 2012; Dojčinović et al., 2016). Plasma degradation of organics can be very effective, however, recently there have been attempts to enhance its efficiency, i.e., to increase energy yield and decrease reaction time by the use of catalysts, like TiO_2 (Ghezzar et al., 2009), tin containing aluminophosphate molecular sieves tin containing aluminophosphate molecular sieves (Hentit et al., 2014) and $BiPO_4$ (Chen et al., 2017) for degradation of organic dyes. Reactive textile azo dye Reactive Black 5 (RB 5) belongs to a large group of colour compounds that are used in colouration industry, which can be found in various wastewaters. Previously, some of the AOPs were applied to degrade RB 5, like DBD plasma (Dojčinović et al., 2016; Mei and Liu, 2013) and catalytic photodegradation with TiO_2 and ZnO/UV slurry membrane reactor (Mahadwad et al., 2011; Becerril-Altamirano et al., 2019; Laohaprapanon et al., 2015), but to the best of our knowledge, there were no attempts with open air atmospheric pressure pulsating corona system, nor any type of plasma process with the use of catalyst. And while many AOPs usually take a lot of energy to complete the degradation process, the use of catalyst can significantly enhance the reaction and thus decrease the reaction time and the energy consumed for the process (Ghezzar et al., 2009).

Zinc molybdenum oxide, $ZnMoO_4$, is a semiconductor with some important applications, like supercapacitor technology (Reddy et al., 2019), optical and electronic devices (Keereeta et al., 2014), catalysis (Wang et al., 2017; Jiang et al., 2014; Ramezani et al., 2015; Oudghiri-Hassani et al., 2018), detection (Rajakumaran

et al., 2020), photocatalytic corrosion protection (Liu et al., 2020), but it was also applied as a sorbent (Oudghiri-Hassani et al., 2018). ZnMoO₄ has shown photocatalytic activity in degradation of some organic compounds, such as Rhodamin B, phenol, sulfamethazine, 3-Nitrophenol, and dyes like Victoria Blue and Methyl Orange (Wang et al., 2017; Jiang et al., 2014; Ramezani et al., 2015; Oudghiri-Hassani et al., 2018), but there are no literature reports, to the best of our knowledge, about its plasma catalytic activity. ZnMoO₄ has different crystalline phases, like α -ZnMoO₄, β -ZnMoO₄ and ZnMoO₄·0.8H₂O (Keereeta et al., 2014), and, depending on the synthesis conditions, it can be micro- or nano-sized, with different crystal shape and morphology (Mahadwad et al., 2011; Becerril-Altamirano et al., 2019; Laohaprapanon et al., 2015; Reddy et al., 2019; Rajakumaran et al., 2020; Jia et al., 2013; Liang et al., 2012; Shahri et al., 2013; Zhai et al., 2017) or in the form of thin films (Askri et al., 2018). Synthesis conditions affect the crystal phase, size and morphology, thus several synthetic routes, with various synthetic conditions have been developed in order to control these features, such as hydrothermal (Jiang et al., 2014; Jia et al., 2013), microwave-hydrothermal (Jiang et al., 2014) and ultrasonication and hydrothermal (Rajakumaran et al., 2020), precipitation (Reddy et al., 2019; Shahri et al., 2013), vapor deposition in air (Zhai et al., 2017), electrochemistry – assisted laser ablation (Liang et al., 2012), spray pyrolysis (Askri et al., 2018) and electrospinning and calcination (Keereeta et al., 2012).

Electrochemical synthesis is very convenient way to obtain various compounds using simple and low cost equipment and starting compounds, with excellent control of synthesis conditions. In this work, for the first time to the best of our knowledge, zinc molybdenum oxide was obtained by galvanostatic electrochemical co-deposition of Zn²⁺ and MoO₄²⁻, followed by thermal treatment and used to enhance plasma-induced

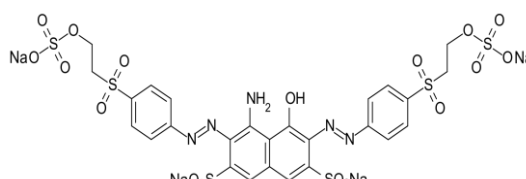
degradation of RB 5. ZnMoO_4 was selected because of its interesting electronic structure, polymorphism, the possibility to control its properties, and previously demonstrated photocatalytic activity and other interesting electronic properties, which all opened the possibility of its exploitation as a plasma degradation catalyst. In this paper, the catalytic degradation of RB 5 by atmospheric pressure non-thermal pulsating plasma corona open air reactor was examined. Characterization and examination of catalytic properties of electrochemically synthesized ZnMoO_4 were done. The interaction of plasma with the ZnMoO_4 catalyst and its role in dye degradation were examined.

2. Experimental

2.1. Materials

Reactive Black 5, $\text{ZnSO}_4 \cdot 7\text{H}_2\text{O}$, $(\text{NH}_4)_6\text{Mo}_7\text{O}_{24} \cdot 4\text{H}_2\text{O}$ and H_2O_2 (Sigma Aldrich) were of reagent grade. All solutions were prepared in deionized water (18 M Ω). Basic characteristics of RB 5 are given in Table 1.

Table 1 Basic characteristics of Reactive Black 5

Dye	Molecular structure	λ_{max} (nm)	Molar mass ($\text{g} \cdot \text{mol}^{-1}$)
Reactive Black 5		597	991.8

2.2. Preparation and characterization of the materials

Working solutions containing $0.008 \text{ mol dm}^{-3}$ $(\text{NH}_4)_6\text{Mo}_7\text{O}_{24}\cdot 4\text{H}_2\text{O}$ and 0.1 mol dm^{-3} $\text{ZnSO}_4\cdot 7\text{H}_2\text{O}$ were prepared by mixing equal volumes of stock solutions of the salts, which were prepared by dissolving required amount of each of the salts separately in deionized water. Solutions concentrations were optimized based on previous experiments. Cyclic voltammograms of stainless steel substrate in the working solution, as well as in pure $0.008 \text{ mol dm}^{-3}$ $(\text{NH}_4)_6\text{Mo}_7\text{O}_{24}\cdot 4\text{H}_2\text{O}$ and 0.1 mol dm^{-3} $\text{ZnSO}_4\cdot 7\text{H}_2\text{O}$, separately, were recorded in three-electrode cell using Palm Sens Em Stat blue potentiostat, stainless steel sheet as a working electrode, Pt as auxiliary electrode and saturated calomel electrode (Amel) as a reference electrode, by cycling at scan rate of 50 mVs^{-1} , from -0.1 to -1.3 V for working solution and $(\text{NH}_4)_6\text{Mo}_7\text{O}_{24}\cdot 4\text{H}_2\text{O}$ solution and from -0.7 to -1.3 for $\text{ZnSO}_4\cdot 7\text{H}_2\text{O}$ solution and in $0.2 \text{ M K}_2\text{SO}_4$ as a background electrolyte. All potentials are given vs standard hydrogen electrode (SHE).

Electrodeposition was done in working solution at pH 5.9 (native pH), using an Amel 510 DC potentiostat (Materials Mates, Italy), furnished by VoltaScope software, at $21 \pm 0.5^\circ\text{C}$ in the two electrode cell with a stainless steel sheet as a substrate (cathode) and a Pt as anode, at two constant current densities of 50 mAcm^{-2} and 100 mAcm^{-2} during 90 minutes. Prior to electrodeposition, the stainless steel substrate was polished with abrasive paper, ultrasonically cleaned with ethanol and rinsed with deionized water. After deposition, for both of the applied current densities, stainless steel cathode covered by dark-gray coat was rinsed with deionized water and dried in air at 50°C . The coat was then peeled of the cathode surface and divided into two parts: the first one did not undergo any further treatment, and the second one was thermally treated at 600°C for 90 minutes in air in a furnace and cooled in open air. This way,

four different materials were obtained and labelled: E50, E100 (obtained by electrodeposition at 50 mA cm^{-2} and 100 mA cm^{-2} , respectively), T50 and T100 (obtained by electrodeposition at 50 mA cm^{-2} and 100 mA cm^{-2} , respectively, and thermally treated at 600°C). These materials underwent characterization and application in dye degradation experiments.

SEM–EDX was done by the JEOL5310LV in low vacuum mode with an Oxford Instruments X-Max 50 detector for semi-quantitative EDX analysis. Nominal magnifications of $\times 5.0 \text{ k}$, 10.0 k and 25.0 k were used when imaging the obtained samples. FTIR spectra were recorded using BOMEMMB-100 FTIR spectrometer (Hartmann & Braun, Canada), with KBr pellets which contained 1.0 mg of the sample/ 150 mg KBr. The instrument was furnished with a standard DTGS/KBr detector in the range of $4000\text{--}400 \text{ cm}^{-1}$ with a resolution of 2 cm^{-1} . XRD characterization was done by the use of filtered $\text{Cu K}\alpha$ radiation (Ultima IV Rigaku). The analysis was carried out in the scan range of $2\theta = 5\text{--}90^\circ$ under 40 kV , 40 mA , with scan rate of 5 degree/min and steps with 0.02° . The standard deviation was about 1% . TG analysis was performed in air atmosphere by heating 2.5 mg of the obtained samples up to 600°C with the heating rate of 2°C/min (TA Instruments TGA 5000IR furnished by Universal Analysis software package). The catalysts' band gap was determined by cyclic voltammetry (Mahmood et al., 2014), applying the same instrumentation as for the electrodeposition.

2.3. Plasma degradations

All plasma degradation experiments were done by the home-made atmospheric pressure non-thermal plasma open reactor, based on positive pulsating corona electrical discharge, using power supply with DC pulse generator and high voltage

output stage (the highest output voltage was 50 kV related to the ground level, maximal power output was 110 W). The liquid surface (treated solutions) acted as a cathode and the multipoint anode with stainless steel needles, was placed above the liquid. The corona discharge occurred on the tip of the needles, in the air phase above the liquid. The reactor cell was of cylindrical shape, with the electric contact at its bottom. The generator frequency was 40 kHz. The discharge current density was set up by changing of the air discharge gap (a distance between the anode and the liquid surface – cathode). During the treatment, gases were removed from the reaction area by the exhaust system. A detail description of the plasma reactor set up is given in (Rančev et al., 2019). The reactor scheme is presented in Figure S1 (supplementary). Plasma treatments were done at temperature of 21 ± 0.5 °C, with 20 cm^3 of each solution, at their native pH of 5.1. Dye concentrations were determined using UV-VIS spectrophotometer Shimadzu UV-1650 PC at 580 nm. Decolourization rate was given as the C/C_0 ratio, where C_0 is the initial dye concentration (mg dm^{-3}) and C is a dye concentration at the reaction time t . Plasma generated H_2O_2 concentration was determined in plasma-treated water, both with and without the use of the catalysts, using iodometric method (Nijadam et al., 2012). The catalysts concentration was 50 mg dm^{-3} . Chemical oxygen demand (COD) was determined by the set up consisting of thermoreactor RD125, the Lovibond® COD Vario tube test and the Lovibond® Multidirect photometer (Lovibond).

3. Results and Discussion

3.1. Characteristics of the synthesized materials

3.1.1. Cyclic voltammetry examination

Cyclic voltammograms of the electrode immersed in the examined solutions are given

in Figure 1. The cycling was done in cathodic direction (from -0.1 to -1.3V for molybdate alone; -0.7 to -1.3V for Zn (II) and from -0.1 to -1.2 for the mixed molybdate – Zn (II) solution) and reversed back to the starting potential.

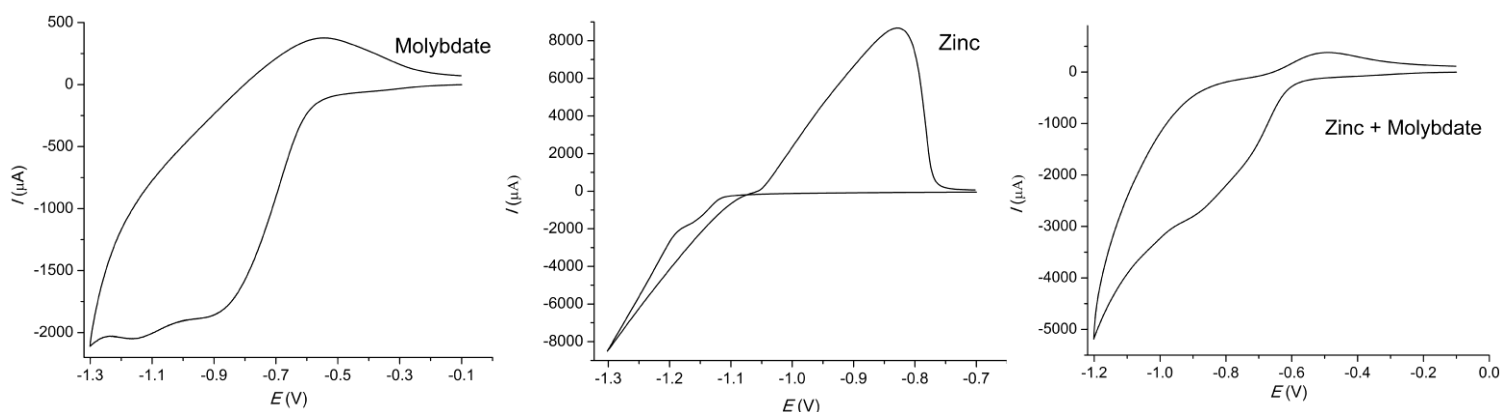


Figure 1 Cyclic voltammogram of Ti-electrode in solution containing $(\text{NH}_4)_6 \text{Mo}_7\text{O}_{24}$, ZnSO_4 and mixture of $(\text{NH}_4)_6 \text{Mo}_7\text{O}_{24}$ and ZnSO_4 in 0.2 M K_2SO_4

In the molybdate solution broad reduction peak observed at about -0.88 V originated from the current caused by the $\text{Mo}_7\text{O}_{24}^{6-}$ ions which were reduced to MoO_2 at that potential (dark MoO_2 coverage could be observed at the electrode surface). The presence of NH_4^+ ions, as well as neutral pH dislocated this peak towards more negative potentials, followed by intensive evolution of H_2 (which took place at the surface of the formed MoO_2), alongside reduction of molybdate (Cao et al., 2019). Broad anodic bend observed at about -0.5 V originated from an oxidation of H_2 , generated during the reduction step (Quintana et al., 2015). In the solution of ZnSO_4 significant increase of cathodic current density at about -1.1 V is attributed to reduction of Zn^{2+} ions to Zn. Small, poorly defined peak at about -1.2 V might originate from H_2 evolution which also takes place in this potential region. Broad

anodic peak with the current maximum at -0.83 V is attributed to oxidation of Zn (Kazimierzak et al., 2020). Cyclic voltammogram recorded in the mix solution which contains both Zn (II) and molybdate, has similar shape to that of the molybdate alone; significant increase of cathodic current starts at about -0.6 V; it continues to increase in cathodic direction in both cases. However, this current is higher in the case of Zn – molybdate mixture: the difference becomes notable at about -0.8 V and it becomes higher for more negative potentials. This current originates from molybdate anions, as well as Zn (II) cations; the current which originates from the late probably occurs at potentials lower than -0.9 V, but it is overlapped by the molybdate band. Anodic peak position and corresponding current density are very similar to those of the molybdate alone, so it attributed to the oxidation of H_2 which originates from reduction of water in the cathodic region. There is no evidence of reversible oxidation of reduced Zn. Base on the cyclic voltammograms and the structure and chemical composition of the obtained product (see below), it is assumed that co-deposition of zinc (II) and molybdate takes place in cathodic region, and that these ions form molybdenum zinc oxide. Some minor deposition of metallic Zn is also possible, but it seems that does not oxidize in the anodic region, like it does in the Zn solution alone.

3.1.2. SEM and EDX analysis

There are some differences in the surface morphology between the obtained materials, especially before and after thermal treatment (Figure 2). Material E50 is composed of mostly oval particles of undefined shape and different size, which varies from 1-2 μm to more than 20 μm . E100 seems sintered, with macro pores, and oval particles of several μm which can be distinguished in places. T50 and T100 have practically the same morphology, with flaky texture, undefined shape and high variation in particle

size, from less than 1 μm to more than 20 μm . In general, the synthesis current density affected the morphology before, but not after the thermal treatment.

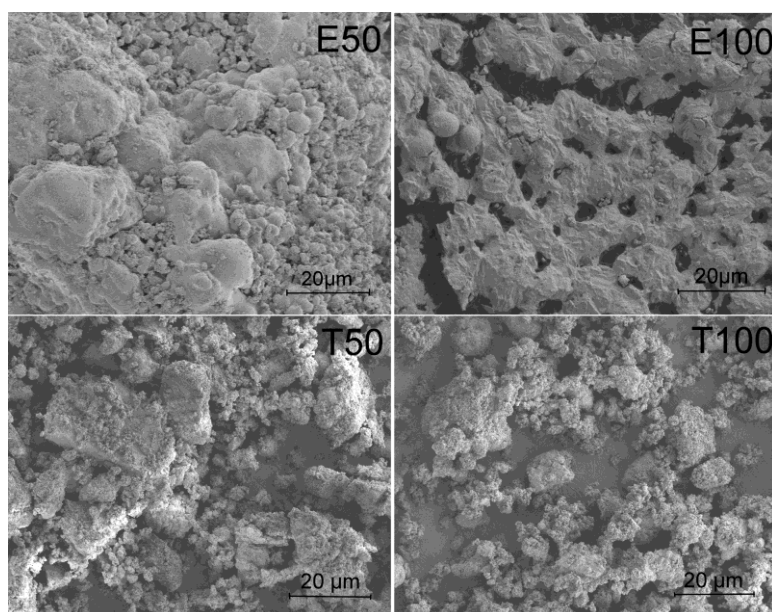


Figure 2 SEM images of the obtained materials

EDX shows the presence of Zn, Mo and O in all four materials in different ratio.

Average atom % of Zn, Mo and O in E50 and E100 is: Zn:Mo:O = 20.6 : 8.29 : 71.11, and 14.55 : 9.21 : 76.24, respectively, which is close to the elements ratio in

molybdenum zinc oxide, $\text{Zn}_5\text{Mo}_2\text{O}_{11}\cdot 5\text{H}_2\text{O}$. However, element distribution is not

uniform, showing the variation of $\pm 7.90\%$ and $\pm 9.50\%$ in E50 and E100, respectively,

which indicates that the materials may not contain only one phase. Average atom % of

Zn, Mo and O in T50 and T100 is: Zn:Mo:O = 16.2 : 13.98 : 69.82, and 15.30 : 12.06 : 72.64, respectively, which, in both cases, approximately corresponds to the elements

ratio in ZnMoO_4 , with little higher content of oxygen and Zn. Element distribution is

more uniform, with variation of $\pm 4.80\%$ and $\pm 5.10\%$ in T50 and T100, respectively.

3.1.3. FTIR spectra analysis

FTIR spectra show significant difference between the compounds before (E50, E100)

and after thermal treatment (T50, T100, Figure 3).

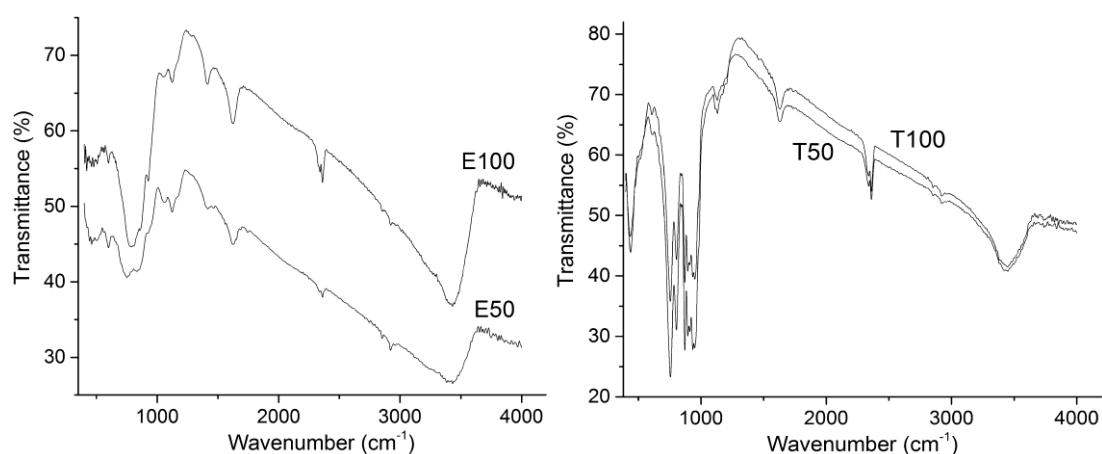


Figure 3 FTIR spectra of the obtained materials

In the spectrum of electrodeposited material E50, a band at 600 cm^{-1} which moves to 608 (FTIR spectrum of T50) and 615 cm^{-1} (FTIR spectrum of T100) after thermal treatment, indicates that O is linked to three metal atoms. The bands at 1460 and 443 cm^{-1} (overlapped by OH deformation, which makes it less visible) indicate O – Zn vibration. Band at 1320 cm^{-1} might be connected with Mo – OH vibration and its disappearance after thermal treatment indicates the change of the initial compound (E50) structure. Band at 1123 cm^{-1} (FTIR spectrum of E50), which most likely originates from some form of crystalhydrate of molybdenum zinc oxide, like $\text{Zn}_5\text{Mo}_2\text{O}_{11}\cdot 5\text{H}_2\text{O}$, moves to 1130 cm^{-1} after thermal treatment (FTIR spectrum of T50). Bands at $1000\text{--}700\text{ cm}^{-1}$ are mainly caused by $[\text{MoOy}]^n$ (Liang et al., 2012). A broad band at 3430 cm^{-1} originates from valence vibration of crystalhydrates OH group, the band at 3300 cm^{-1} from vibration of OH group from H_2O molecules (but it may also originate from NH_4^+) and the small bands between 1630 and 1650 cm^{-1} from deformation OH vibration in plane of H_2O molecules due to the presence of various crystalhydrates. Band at 1060 cm^{-1} is connected with valence S – O vibration, indicating some residual sulfate, which disappears after thermal treatment, along with

H₂O molecules. Comparison of the E50 and T50 spectra show that ZnMoO₄ was not detected in E50 sample, which suggests, along with the previous findings, that E50 is some hydrated form of molybdenum zinc oxide of undefined structure, with traces of impurities from starting compounds. FTIR spectrum of E100 is very similar to that of E50, so, it will not be discussed separately.

FTIR spectrum of T50 shows sharp, intensive bands in the range 1000 – 700 cm⁻¹.

The bend at 950 cm⁻¹ indicates symmetric valence Mo – O vibration (ν_1 stretching) from Mo – O – Mo bonding. Band at 870 cm⁻¹ corresponds to asymmetric valence (ν_3 stretching) Mo – O vibration from (MoO₄)²⁻ tetrahedron units. Doublet at 895 and 910 cm⁻¹ confirms the presence of (MoO₄)²⁻ tetrahedron. Sharp peaks at 805 and 871 cm⁻¹, as well as the group of intensive sharp peaks in the range of 950 – 870 cm⁻¹ indicate Mo – O vibration typical for B_{2U} and B_{3U} symmetry at the compounds of [MoO_y]ⁿ⁻ type. The band at 755 cm⁻¹ originates from valence (ν_3 stretching) Mo – O vibration. This is a clear evidence of the existence of (MoO₄)²⁻ tetrahedron. Intensive and sharp band at 435 cm⁻¹ originates from valence Zn – O bond, which, altogether with the band at 1460 cm⁻¹ (Zn – O vibration) confirms the presence of ZnMoO₄ (Shahri et al., 2013: , 28 Keereeta et al., 2012). FTIR spectrum of T100 is very similar to that of T50, indicating basically the same main compound, so, it will not be separately discussed.

3.1.4. XRD analysis

Significant differences are observed in XRD pattern, especially between electrodeposited only and thermally treated materials (Figure 4).

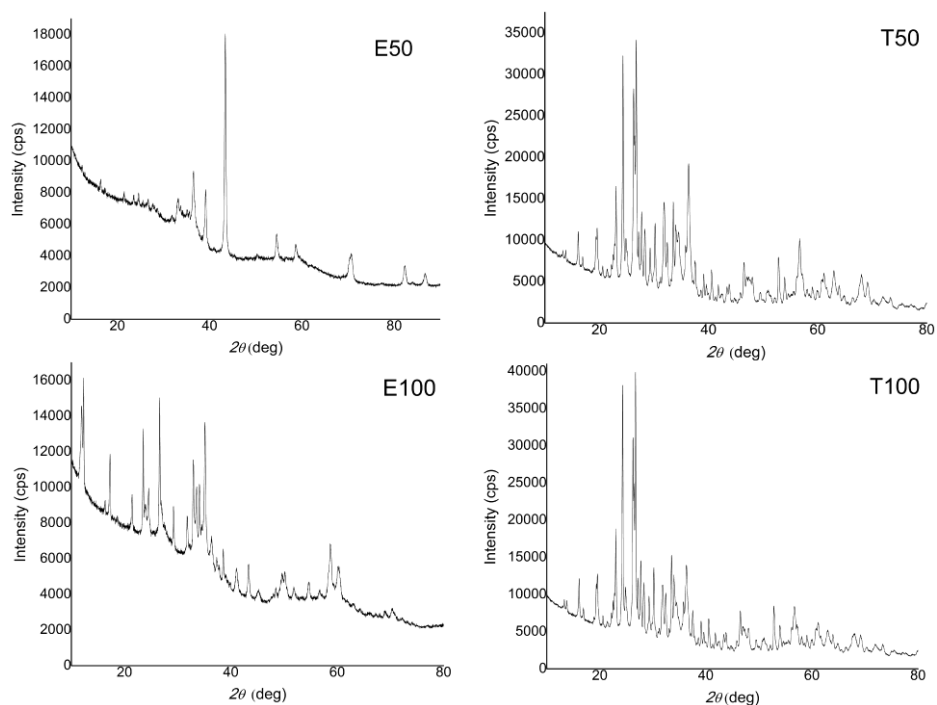


Figure 4 XRD pattern of the obtained materials

E50 is amorphous, and the only crystal phases detected by XRD are small amount of metallic Zn (hexagonal space group 194: $P6_3/mmc$, main peak at $2\theta = 43.5^\circ$), which was co-deposited at the cathode, and the residual $ZnSO_4(OH)_6 \cdot 5H_2O$ (triclinic space group 2: P1). E100 contains certain amount of amorphous phase, but the dominant phase is crystalline Zinc Molybdenum Oxide Hydrate, $Zn_5Mo_2O_{11} \cdot 5H_2O$ (rhombohedral space system 147: P3, with lattice parameters $a = b = 6.13 \text{ \AA}$, $c = 21.71 \text{ \AA}$, $V = 706.4 \text{ \AA}^3$, angles $\alpha = \beta = 90.0^\circ$ and $\chi = 120.0^\circ$ (JCPDS 30-1486)), with characteristic, intensive and well defined peaks at $2\theta = 12.34^\circ$, 17.35° , 23.53° , 26.63° and 29.06° , which do not appear in the pattern of E50. Traces of $ZnSO_4(OH)_6 \cdot 5H_2O$ are detected in T100 as well, but there is no evidence of the presence of metallic Zn; E100 was obtained at higher current density, which means more negative local cathodic potential, and more intensive evolution of H_2 and OH^- , which reacted with oncoming Zn^{2+} ions leading to formation of Zn(II) hydroxide, rather than metallic Zn.

XRD patterns of T50 and T100 are similar. Both materials are well crystalline, with sharp, well defined peaks. XRD pattern of T50 shows that it is triclinic (α) ZnMoO_4 (space group 2: P-1), with lattice parameters $a = 8.33 \text{ \AA}$, $b = 9.65 \text{ \AA}$, $c = 6.94 \text{ \AA}$, $V = 513.82 \text{ \AA}^3$, angles $\alpha = 106.9^\circ$, $\beta = 101.72^\circ$ and $\gamma = 96.73^\circ$ (JCPDS 35-0765). Diffraction peaks are positioned at 13.25, 16.0, 19.29, 22.72, 24.23, 26.69, 27.57, 30.1, 32.40, 33.40 and 33.45°. XRD pattern of T100 shows that is composed of triclinic ZnMoO_4 as well, with basically the same lattice parameters. It can be assumed that the current density affected the crystallinity of electrodeposited material, but it has no effect of its structure after thermal treatment. Though XRD pattern of E50 does not show peaks of any molybdenum compound due to its amorphicity, it is assumed (based on the structures after thermal treatment) that it also some form of molybdenum zinc oxide.

3.1.5. TG analysis

Thermographs of electrodeposited materials (E50 and E100) have similar shape and they show significant weight change during heating up to 600°C, indicating chemical change (Figure 5). The weight of the heated samples decreases up to about 273.5°C and 255.4°C for E50 and E100, respectively; after that, it shows a slight increase. The total corresponding weight loss at those points is 11.30% and 12.8%, respectively, which is close enough to the loss of crystal water in $\text{Zn}_5\text{Mo}_2\text{O}_{11} \cdot 5\text{H}_2\text{O}$ (11.54%) (Liang et al., 2012). Thus, it can be assumed that the major processes during heating is dehydration of $\text{Zn}_5\text{Mo}_2\text{O}_{11} \cdot 5\text{H}_2\text{O}$ which is finished at about 255-274°C, and, after that, a phase transformation to triclinic ZnMoO_4 , which takes place up to 600°C without chemical weight loss. Thermographs of thermally treated materials do not show any significant change (T50 and T100) in the heating range, showing chemical

stability of the obtained ZnMoO_4 . Small weight loss of less than 1% up to about 120-150°C is attributed to the loss of adsorbed water or gases.

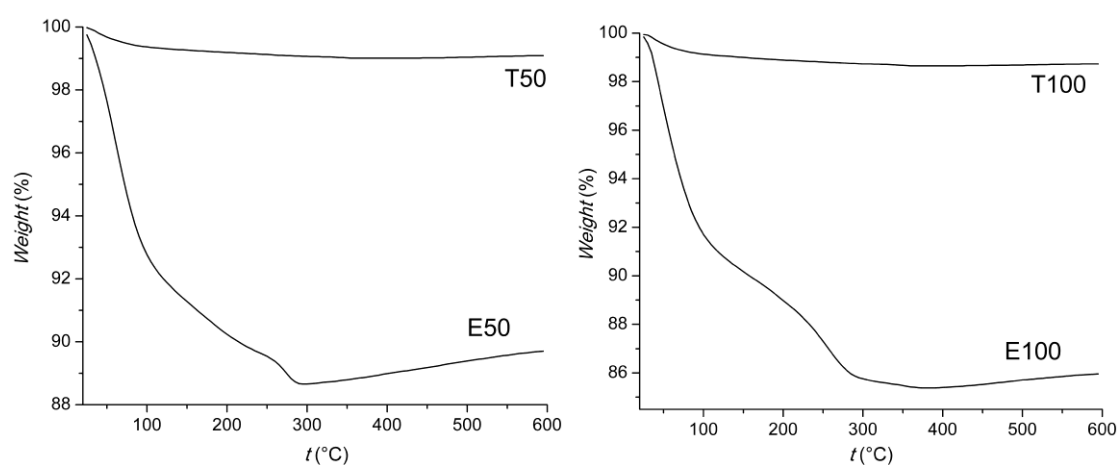


Figure 5 Thermographs of the obtained materials

Based on all the findings, it can be assumed that electrodeposition had led to a formation of molybdenum zinc oxide, $\text{Zn}_5\text{Mo}_2\text{O}_{11}\cdot 5\text{H}_2\text{O}$, which was later thermally transformed to triclinic ZnMoO_4 . Electrodeposition current density affected crystal structure and slightly affected surface morphology and elemental composition of electrodeposited material. It slightly affected elemental composition of thermally treated material, but basically did not affect its surface morphology and crystal structure. Both T50 and T100 are triclinic ZnMoO_4 , with practically the same morphology.

3.2. Plasma-catalytic degradation

RB 5 is resistant to oxidants such as O_2 , and H_2O_2 . It was also stable when exposed to UV radiation alone. When exposed to plasma, relatively fast decolorization was observed, especially in presence of some of the tested catalysts. E50 and E100 practically did not show catalytic activity towards plasma decolorization of 25 mg dm^{-3} solution of Reactive Black 5, i.e., decolourization rate was the same as with plasma

alone. The reason is probably their poor crystallinity, which acted like electron – holes recombination centers, decreasing the possibility of their reaction with the liquid phase (Wang et al., 2017) (Figure 6).

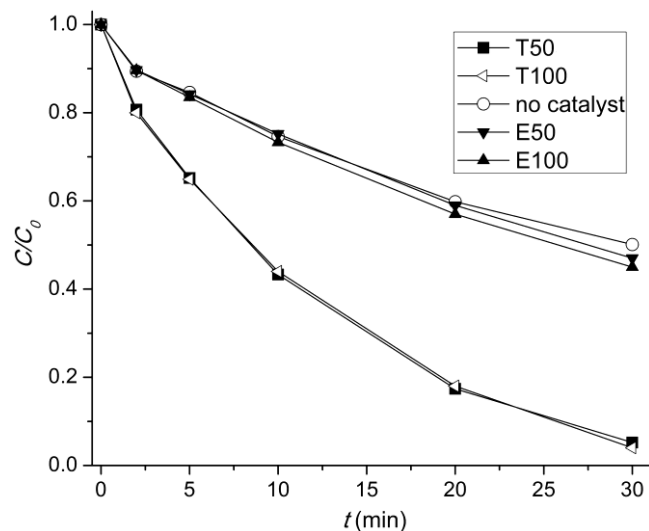


Figure 6 Plasma decolorization of RB 5 solution with the use of synthesized catalysts and without the catalyst.

T50 and T100 exhibited plasma-catalytic activity: 50% decolorization was achieved more than 3 times faster than with plasma alone. Furthermore, after 30 minutes of the treatment, 95% of decolorization was achieved with the catalyst, while it was about 50% without it. Since the difference in catalytic activity between T50 and T100 were negligible, T50 was chosen as the catalyst in further examination and optimization because it was obtained at lower current density. In further text, this material will be referred to as MoZnO_4 . Its determined band gap was 3.39 eV. It was micro crystalline and easy to separate from liquid phase. After five consecutive runs and regenerations (drying in open air), it kept 95.5% of its catalytic activity.

3.2.1. Formation, decomposition and consumption of H_2O_2 during the plasma process

During the plasma treatment, content of H₂O₂ increased both in the water alone, dye solution alone, water with the addition of catalyst, as well as in dye solution with the addition of catalyst (Figure 7).

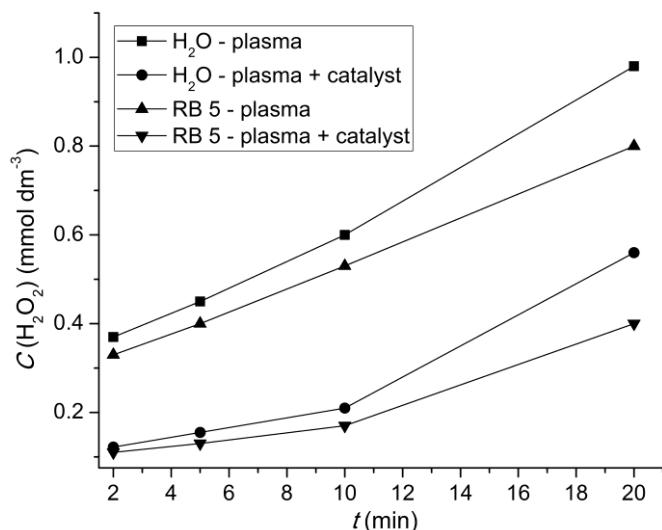
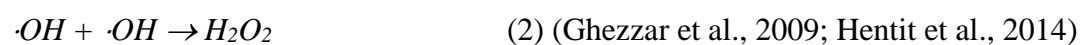
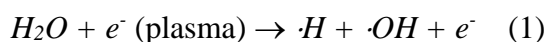


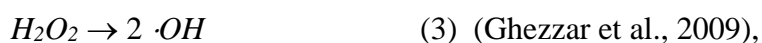
Figure 7 Concentration of H₂O₂ in plasma treated water and RB 5 solution with and without ZnMoO₄ catalyst.

In all four cases, a strong electric field between multipoint anode and liquid surface – cathode, caused the creation of reactive species and UV radiation in the air between them. When the fast plasma – generated electrons and reactive oxygen species (various radicals), accelerated by the strong electric field, hit the liquid surface, many chemical reactions occurred; H₂O₂ can be formed as a product of some of them, according to the equations:



In the absence of the catalyst in the system, the increase of H₂O₂ concentration in function of the treatment time was linear, both in water and in dye solution. H₂O₂ content was lower in dye solution than that in water during all the treatment time, and the difference became more significant as the treatment time increased. This implies that H₂O₂ was involved in decolourization reactions, i.e., that it was consumed as a reagent in dye degradation.

Once formed by the action of plasma, H₂O₂ can further undergo decomposition, caused by plasma treatment as well, which results in the formation of short-live active oxygen species, like hydroxyl radical, ·OH



Hydroxyl radical practically only exists during the treatment and it possesses very high oxidative potential, high enough to oxidize the dye. To investigate the roll of ·OH radical in dye degradation, a trapping agent for ·OH radical, DMSO, was added to a system and only a small % of decolourization (less than 10% in 30 minutes of the treatment both with and without the catalyst) was observed. Thus, all the three experimental findings (increased decolourization with the increase of H₂O₂, lower content of H₂O₂ in dye solution compared to water and a sharp drop of decolourization rate in the presence of DMSO), as well as the findings from literature, strongly indicate that the principle decolourization reagent was ·OH radical.

3.2.1.1. Role of the catalyst in plasma degradation of a dye

As shown in Figure 7, H₂O₂ was formed during the plasma treatment in the system with catalyst, both in water and in dye solution. Its concentration was significantly

lower than that in the absence of a catalyst and it increased slower. It is evident that the catalyst interacted with plasma-generated H_2O_2 . The pulsating positive corona discharge applied in these experiments was generated at relatively high frequency, without the occurrence of sparks and with the appearance of relatively low-intensity streamers, providing UV radiation and active electrons and radical species (Rančev et al., 2019). Like the water molecules, catalyst could also be excited when hit by plasma generated active species (mostly positive ions and radicals) in the liquid surface area (plasma-generated ion wind provided an intense constant stirring and uniform distribution of the catalyst particles during the treatment). These active species, accelerated by the strong electric field, hit the semiconducting catalyst, and if they possessed the energy higher than the band gap of the catalyst, that energy was likely transferred from the active species to the catalyst, causing its excitation, i.e., creation of electron (e^-) – positive holes (h^+) pairs (Bogaerts et al., 2020; Kim et al., 2005; Abroyan et al., 1967). It was shown in literature that electron (e^-) – positive holes (h^+) pairs were created in ZnMoO_4 by UV light excitation, which caused its photocatalytic activity (Ramezani et al., 2015). However, the measurement showed that the intensity of generated UV light in our case was relatively low, so that was not the principle way of excitation, but rather high energy corona-generated species. In addition, a number of streamers which reached the liquid surface through the air gap, provided more reactive species with energies of up to 10 eV which could excite the semiconducting ZnMoO_4 catalyst and create the electron (e^-) – positive holes (h^+) pairs (i.e., those of them with the energy higher than the material's band gap) (Bruggeman et al., 2016; Sato et al., 2008). The detailed corona discharge characterization is given in (Petrović et al., 2021). Once created, short living e^- and h^+ reacted with the plasma-generated H_2O_2 , which lead to a formation of more $\cdot\text{OH}$

radical (equations 7 and 8).

These ·OH radicals reacted with the dye molecules and contributed to its degradation.

In the system with the catalyst, the content of H₂O₂ in the dye solution was lower than that in the water, just like in the system without the catalyst (Figure 7), meaning that

in this case, ·OH were consumed in the process of dye degradation as well. So,

basically, the role of the ZnMoO₄ catalyst in this process was to enhance the

production of the main dye degradation reagent, ·OH radical, by decomposing H₂O₂ in

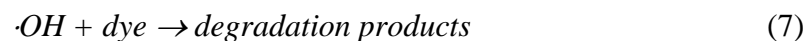
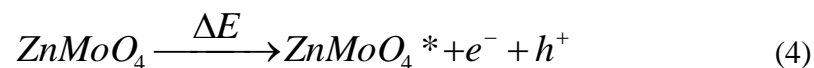
its reaction with e⁻ and h⁺ formed when the plasma generated reactive species with the

sufficient energy stroke the catalyst. It is very likely that UV radiation also took part

in the excitation process, but much less than high energy species from ionized air

(Sato et al., 2008). This can be briefly presented by the equations (Wang et al., 2017;

Ghezzar et al., 2009; Ramezani et al., 2015):



Where ΔE represents energy provided by the strikes of high energy species or UV radiation generated by plasma.

3.2.2. Kinetics of plasma catalytic decolorization

Plasma catalytic decolourization is best described by the pseudo – first order kinetics model (Figure 8), which is represented by the equation 7:

$$\ln(C/C_0) = -kt \quad \text{eq. (7),}$$

where C_0 is initial dye concentration, C is a dye concentration after reaction time t , and k is the reaction rate constant (min^{-1}). The plot of $\ln(C/C_0)$ against time scale is linear in whole examined concentration range, with the values of coefficient of determination, R^2 , higher than 0.99, strongly indicating good agreement with the pseudo first order kinetics (Table 2). This kinetics model was reported by other group of authors as well for the plasma catalytic decolourization (Chen et al., 2017).

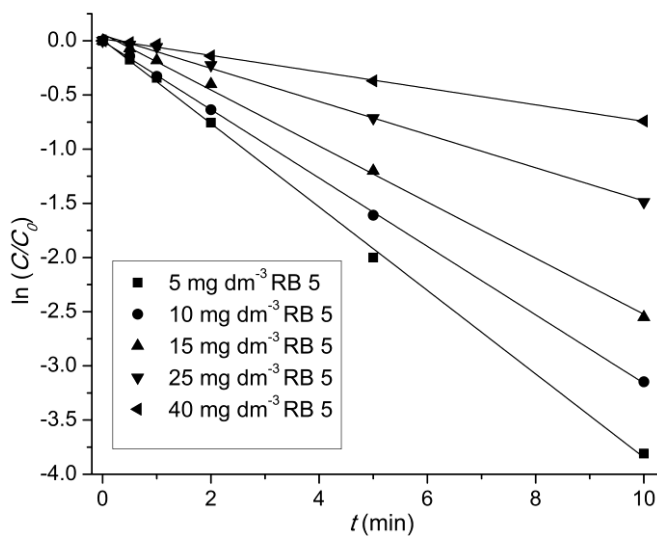


Figure 8 Pseudo – first order kinetics of plasma catalytic degradation of RB 5

Table 2 Reaction rate constants and coefficient of determination (R^2) values for pseudo – first order kinetics of plasma catalytic reactions

	Plasma + 50 mg dm ⁻³ ZnMoO ₄	
C_0 (mg dm ⁻³)	R^2	k_f (min ⁻¹)
5	0.998	0.385
10	0.998	0.316
15	0.997	0.259
25	0.995	0.153
40	0.994	0.080

Table 2 shows that the reaction rate constant decreased with the increase of the initial dye concentration and that dependence was more significant at higher initial concentrations. The reason is probably the ratio between $\cdot\text{OH}$ radicals and dye molecules concentration, which became less favorable with the increase of initial dye concentration (while the $\cdot\text{OH}$ concentration remains constant). The other reason is defragmentation of the dye molecule as the plasma treatment progressed, which further consumed $\cdot\text{OH}$ radicals and it took more time to complete the reactions. The reaction rate constant for the non catalyzed plasma degradation of 25 mg dm⁻³ RB 5 was 0.020 min⁻¹ under the same conditions, which means that the catalyzed reaction's rate was about 7.5 times higher than that of the non catalyzed one. Thus, the presence of the catalyst significantly improved the process by the mechanism described in details in 3.2.1.1.

3.2.3. Effect of discharge current density

The discharge current density (j) between multipoint anode and liquid surface (cathode) was set up by changing the distance (d) between them; j decreased with the

increase of d . Decolourization rate increased with the increase of j (Figure 9).

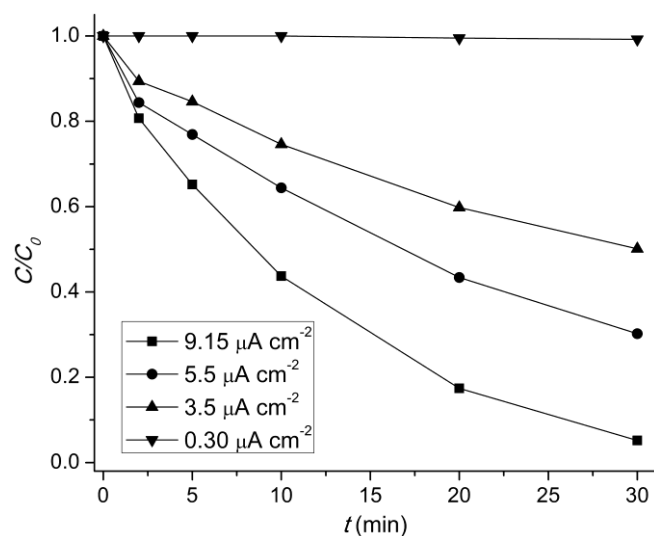


Figure 9 Effect of discharge current density on plasma catalytic decolourization of RB

5.

The increase of current density means the increase of the electric field intensity, which thus provided more energy for acceleration of ions in air and, consequently, facilitated diffusion of reactive species into solution, which affected the decolourization rate (Rančev et al., 2019). H_2O_2 content in plasma – treated water, both with and without the catalyst, increased with the increase of j (Figure 10). It increased in the same manner in all the examined range of j and its increase is in correlation with RB 5 decolourization.

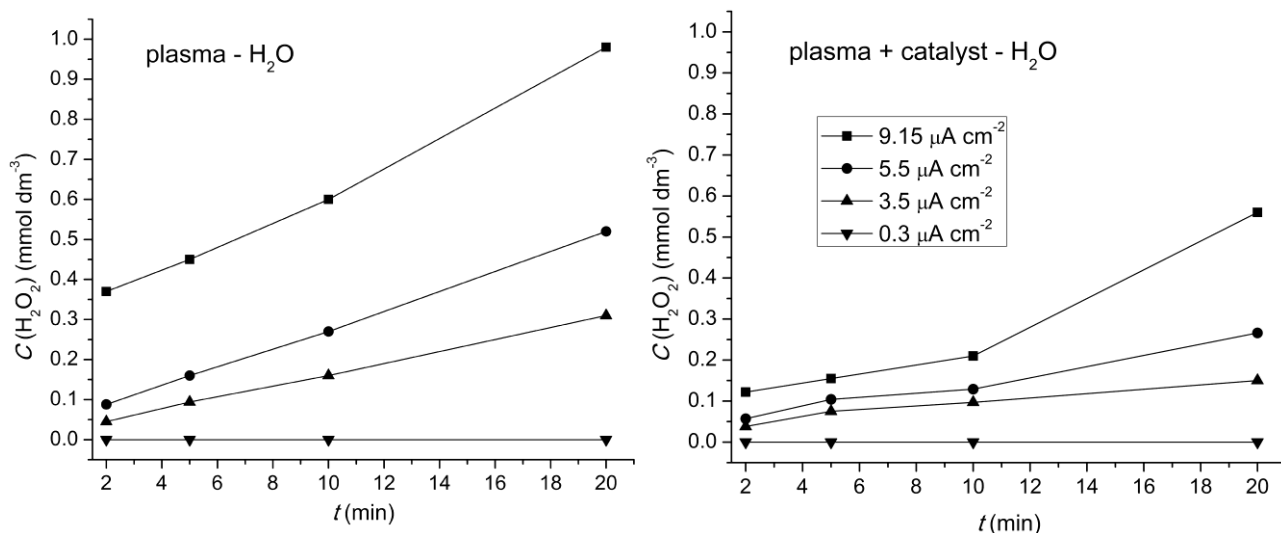


Figure 10 Effect of current density on concentration of plasma - generated H_2O_2 in treated water with and without the ZnMoO_4 catalyst

Maximal j which provided a stable corona discharge was $9.15 \mu\text{A cm}^{-2}$. At this current density, decolourization rate is the highest, as well as the content of H_2O_2 , so it was chosen as an optimal current density. For $j = 0.3 \mu\text{A cm}^{-2}$ or lower, the discharge disappeared, and consequently, the H_2O_2 and decolourization were not detected. For $j > 9.15 \mu\text{A cm}^{-2}$, corona discharge became unstable, with the appearance of sparks.

3.2.4. Effect of initial pH

The highest decolourization rate was observed at the initial dye solution native pH of 5.1, it was little lower in acidic and significantly lower in basic medium, although it was relatively high even at that pH (Figure 11). Slight decrease of decolourization rate at pH 3 was probably caused by protonation of the reactive species, and its decrease at pH 10 by the scavenging effect of OH^- ions. Similar effect of pH on non-thermal plasma degradation of Methyl Orange in circulatory air tight reactor was reported by Jiang et al. (Jiang et al., 2012), but the other work it was found that pH had no effect upon degradation of RB 5 by DBD non-thermal plasma reactor (Dojčinović et al.,

2016).

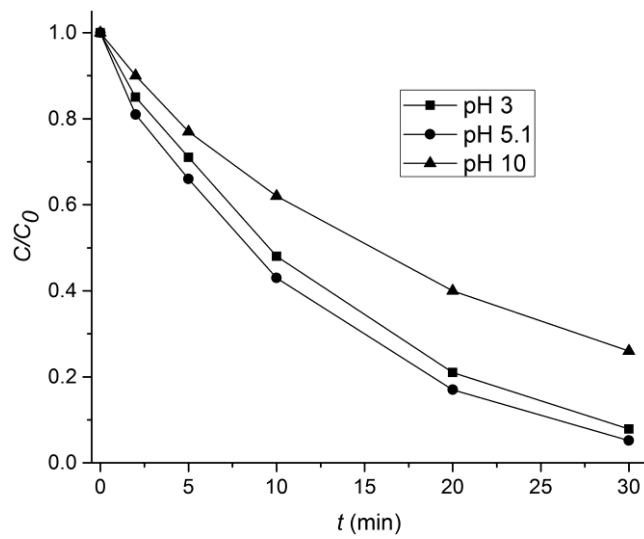


Figure 11 Effect of initial pH on plasma catalytic decolourization of RB 5

3.2.5. Effect of the reactor input voltage

Decolourization rate increased with the increase of the reactor input voltage (Figure 12).

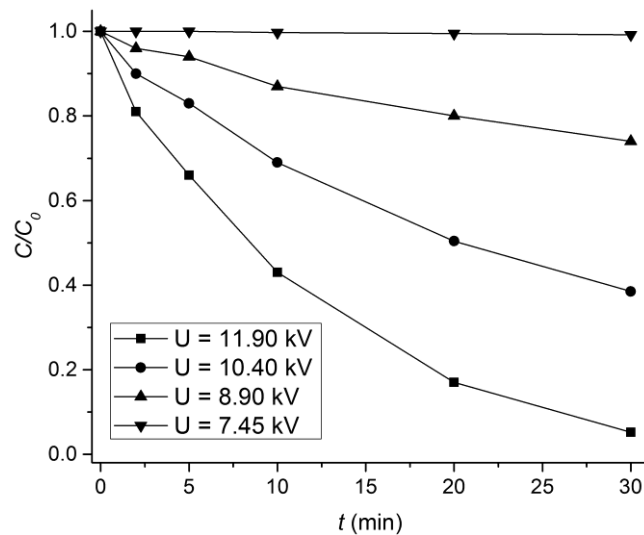


Figure 12 Effect of the reactor input voltage on the plasma catalytic decolourization of RB 5

The voltages which could induce the gas discharge, i.e., the appearance of plasma

corona were higher than 7.45 kV. At the voltages equal or lower than 7.45 kV, corona disappeared and that directly affected the decolourization rate, which dropped to zero, i.e., it did not happen, even after the 4 hours of the treatment. This further proves that the gas discharge, i.e., creation of the reactive species, is necessary to happen and that the input voltage between anode and liquid cathode itself is not enough to induce the decolorization. The highest decolourization rate was observed at 11.90 kV and that was set as the optimal voltage for the process. For the voltage higher than 11.90 kV, the sparks started to appear. Decrease of the voltage caused the decrease of the number of reactive species and the decrease of the electric field which accelerated them, and that affected the decolourization rate.

3.2.6. Effect of the reactor cell dimensions

Three reactor cells of cylindrical shape with different radius were tested in order to investigate the effect of the ratio between the cell radius, d (mm) and the height of the liquid level in the cell, h (mm). Total volume of the treated dye solution was equal for all the three cells. The examined ratio d/h ranges from 2 to 18. The reactor cells dimensions were chosen based on how they physically fitted the overall setup for the examined amount of liquid. Figure 13 shows that d/h ratio had negligible effect upon plasma catalytic decolourization of RB 5, which implies that it did not affect the effectiveness of pulsating corona discharge; so, in this case, it was a minor parameter. The cell with $d/h = 6$ was chosen for other experiments due to the practical reasons.

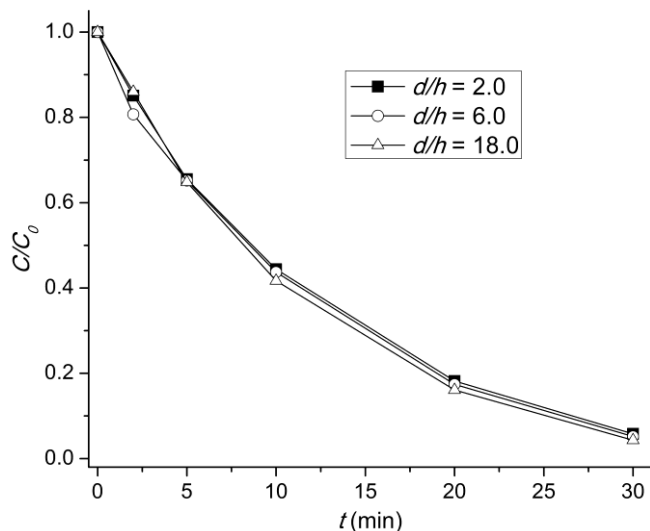


Figure 13 Effect of the d/h ratio on plasma catalytic decolourization of RB 5

3.2.7. Energy yield

One of the goals of using a catalyst was to increase energy yield, which is related to energetic efficacy of the process. Figure 14 shows energy yield, expressed as the mass of the degraded dye (g) for the consumed source energy (kWh) in the function of treatment time. It is evident that energy yield is significantly higher for the catalysed process.

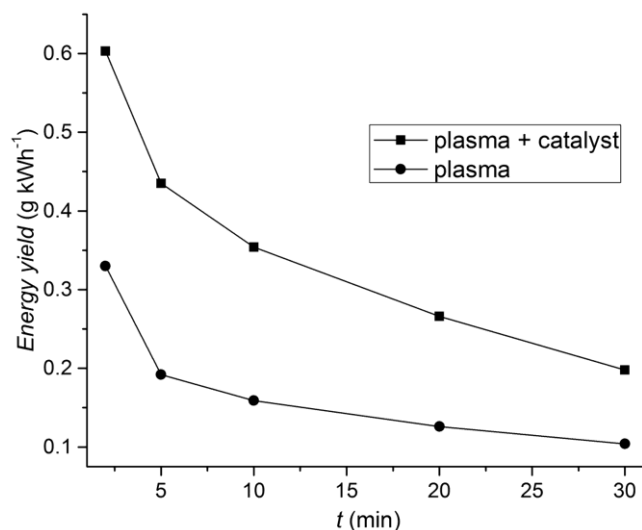


Figure 14 Energy yield in the function of treatment time for catalysed and non – catalysed plasma decolourization of RB 5

For example, it takes 30 minutes to degrade 50% of the dye without and 8.5 minutes with the catalyst (Figure 6). It means that the energy yield for decolourization of 50% of a dye is and 0.10 (gkWh⁻¹) and 0.46 (gkWh⁻¹) for the non – catalysed and catalysed process, respectively. So, the use of a catalyst significantly decreased the power consumption for the process.

Energy yield for 50% decolourization was chosen as a reference value for easier comparison with literature data. It rapidly increases with the increase of initial dye concentration, especially in the range of lower C_0 and it reaches its maximum of 1.86 gkWh⁻¹ for C_0 of about 400 mg dm⁻³ (Figure 15).

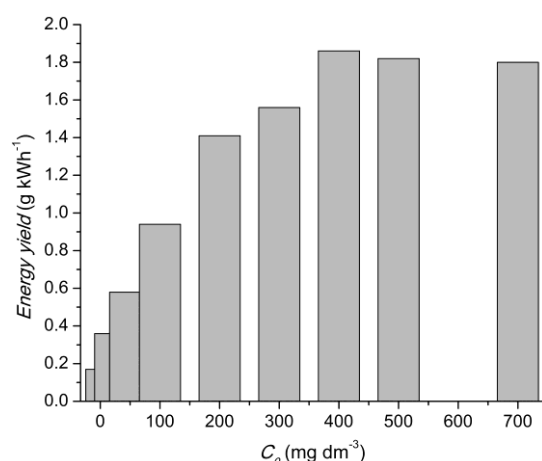


Figure 15 Energy yield for 50% plasma catalytic decolourization of RB 5 as a function of its initial concentration

For comparison to the literature data for various dyes and systems, the maximal energy yield achieved with the same system for RB 19 decolourization with MoO₃ catalyst was 1.48 g kWh⁻¹ (Petrović et al., 2021), 0.482 – 0.650 g kWh⁻¹ for Indigo Carmine by pulsed high voltage discharge in air (Ruma et al., 2018), 0.45, 0.44 and 11.68 gkWh⁻¹ for Methyl Orange by pulsed high voltage discharge in air (Sun et al.,

2012), pulse diaphragm discharge with air bubbling [(Zhang et al., 2009) and non-thermal plasma advanced oxidation in a circulatory airtight reactor (Magureanu et al., 2015) respectively and 0.4 and 0.037 g kWh⁻¹ for Methylene Blue by atmospheric pressure non-thermal plasma jet (Chandana et al., 2015) and by microwave atmospheric pressure plasma jet (García et al., 2017) . So far, we did not find the literature data about energy yield for degradation of RB 5 by some plasma process, but in photodegradation of RB 5 in a ZnO/UV slurry membrane reactor the energy consumption for 95% colour removal was 1.62 kWh g⁻¹, i.e., the energy yield was 0.617 g kWh⁻¹ (Becerril-Altamirano et al., 2019).

3.2.8. Total organic carbon (TOC) removal

After decolourization was completed, the prolonged plasma treatment up to 180 minutes brought a significant decrease of TOC, which reached 81.5% and 85.4% after 120 and 180 minutes, respectively (Figure 16). This means that within 2 or 3 hours, a significant mineralization of the starting compound was attained.

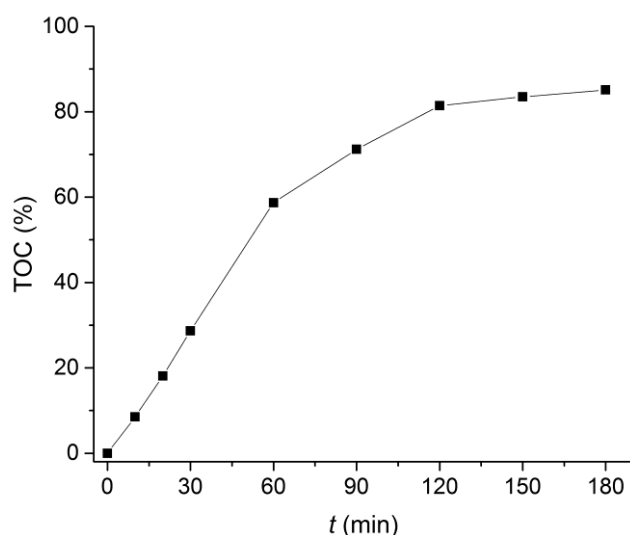


Figure 16 TOC removal by catalytic plasma treatment of RB 5.

4. Conclusion

ZnMoO₄ was synthesized by electrodeposition from the solution containing Zn²⁺ and MoO₄²⁻ ions, followed by thermal treatment. Electrodeposition provided Zinc Molybdenum oxide, Zn₅Mo₂O₁₁•5H₂O; the applied current density affected the crystallinity and morphology of the deposited material. The obtained Zn₅Mo₂O₁₁•5H₂O was thermally transformed to α-ZnMoO₄, and the electrodeposition current density did not affect the final characteristics of thermally treated compound. It was applied as a catalyst for degradation of RB 5 by open air atmospheric pressure pulsating corona plasma reactor. Constant rate of the catalyzed decolourization reaction was 7.5 times higher than non-catalyzed one. The role of the catalyst was to enhance generation of ·OH radical, the principle degradation reagent, by enhancing decomposition of plasma – generated H₂O₂. The catalyst was mostly excited by the strikes of plasma – generated active species accelerated by the electric field, which transferred their energy to the catalyst and, if it was higher than its band gap, the electron – holes pairs were created and reacted with H₂O₂, forming ·OH radicals. Decolourization reactions followed pseudo – first order kinetics. Decolourization rate increased with the increase of the discharge current density and the reactor input voltage. It was the fastest in weakly acidic – neutral pH. Ratio between cylindrical cell radius and the height of the liquid level in the cell did not affect decolourization rate. Energy yield for 50% decolourization was 1.86 gkWh⁻¹. After 180 minutes of the treatment, the TOC removal was 85.4%, which indicates relatively high mineralization.

Acknowledgement

The authors would like to acknowledge financial support from the Ministry of

Reference

- [1] Abroyan, A., Ereemeev, M.A., Petrov, N.N. 1967. Excitation of electrons in solids by relatively slow atomic particles. *Sov. Phys. Usp.* 10, 332 – 367.
- [2] Askri, B., Mhamdi, A., Mahdhi, N., Amlouk, M. 2018. Growth and physical investigations of sprayed ZnMoO₄ thin films along with wettability tests, *Phys. B* 539, 51–60, <https://doi.org/10.1016/j.physb.2018.03.051>
- [3] Becerril-Altamirano, N.L. Hernández López, R.T., González Reyes, L., Suárez Parra, A.R., Ramírez López, R., Martínez Jiménez, A., Hernández-Pérez, I. 2019. Reactive Black-5 Photodegradation by TiO₂ Thin Films Prepared by Ultrasonic Spray, *Journal of Physics: Conf. Series* 1221, 012027, doi:10.1088/1742-6596/1221/1/012027
- [4] Bogaerts, A., Tu, X., Whitehead, R.C., Centi, G., Lefferts, L., Guaitella, O., Azzolina-Jury, F., Kim, H., Murphy, A.B., Schneide, W.F., Nazaki, T., Hicks, J.S., Rousseau, A., Thevenet, F., Khacef, A., Carreon, M. 2020. The 2020 plasma catalysis roadmap, *J. Phys. D: Appl. Phys.* 53, 443001 (51pp). <https://doi.org/10.1088/1361-6463/ab9048>
- [5] Bruggeman P.J. et al. 2016. Plasma–liquid interactions: a review and roadmap, *Plasma Sources Sci. Technol.* 25, 053002 – 59. doi:10.1088/0963-0252/25/5/053002
- [6] Cao, H., Tong, C., Zhang, H., Zheng, G. 2019. Mechanism of MoO₂ electrodeposition from ammonium molybdate solution, *Trans. Nonferrous Met. Soc. China* 29, 1744–1752. <https://doi.org/10.1016/S1003->

- [7] Chandana, L., Manoj Kumar Reddy, P., Subrahmanyam, C.,
2015. Atmospheric pressure non-thermal plasma jet for the degradation of
methylene blue in aqueous medium, Chem. Eng. J. 282, 116–122.
<http://dx.doi.org/10.1016/j.cej.2015.02.027>
- [8] Chen, J., Du, Y., Shen, Z., Lu, S., Su, K., Yuan, S., Hu, Z., Zhang, A., Feng,
J. 2017. Non-thermal plasma and BiPO₄ induced degradation of aqueous
crystal violet, Sep. Purif. Technol. 179, 135–14.
<http://dx.doi.org/10.1016/j.seppur.2017.02.007>
- [9] Dojčinović, B.P., Obradović, B.M., Kuraica, M.M., Pergal, M.V., Dolić, S.D.,
Indić, D.R., Tosti, T.B., Manojlović, D.D. 2016. Application of non-thermal
plasma reactor for degradation and detoxification of high concentrations of
dye Reactive Black 5 in water, J. Serb. Chem. Soc. 81, 829–845, doi:
10.2298/JSC160105030D
- [10] García, M.C., Mora, M., Esquivel D., Foster, J.E., Rodero A., Jimenez-
Sanchidri, C., Romero-Salguero, F.J. 2017. Microwave atmospheric pressure
plasma jets for wastewater treatment: Degradation of methylene blue as a
model dye, Chemosphere 180, 239 - 246.
<http://dx.doi.org/10.1016/j.chemosphere.2017.03.126>
- [11] Ghezzar, M.R., Abdelmalek, F., Belhadj, M., Benderdouche, N.,
Addou, A. 2009. Enhancement of the bleaching and degradation of textile
wastewaters by Gliding arc discharge plasma in the presence of TiO₂ catalyst,
J. Hazard. Mater. 164, 1266–1274.
<https://doi.org/10.1016/j.jhazmat.2008.09.060>
- [12] Hentit, H., Ghezzar, M.R., Womesc, M., Jumas, J.C., Addou, A.,

- Ouali, M.S. 2014. Plasma-catalytic degradation of anthraquinonic acid green 25 in solution by gliding arc discharge plasma in the presence of tin containing aluminophosphate molecular sieves, *J. Mol. Catal. A: Chem.* 39, 37–44. <http://dx.doi.org/10.1016/j.molcata.2014.03.003>
<https://doi.org/10.1002/ppap.201700176>
- [13] Jia, R., Zhang, C., Xu, J. 2013. Morphology-Controllable Synthesis and Characterization of ZnMoO₄ Nanoparticles, *Adv. Mat. Res.* 624, 51-54, doi:10.4028/www.scientific.net/AMR.624.51
- [14] Jiang, B., Zheng, J., Liu, Q. 2012. Wu M., Degradation of azo dye using non-thermal plasma advanced oxidation process in a circulatory airtight reactor system, *Chem. Eng. J.*, 204 – 206, 32 – 39, <http://dx.doi.org/10.1016/j.cej.2012.07.088>
- [15] Jiang, Y.-R., Lee, W. W., Chen, K.-T., Wang, M.-C., Chang, K.-H., Chen, C.-C. 2014. Hydrothermal synthesis of β-ZnMoO₄ crystals and their photocatalytic degradation of Victoria Blue R and phenol, *J. Taiwan. Inst. Chem. Eng.* 45, 207–218, <http://dx.doi.org/10.1016/j.jtice.2013.05.007>
- [16] Kazimierczak, K., Swiaćtek, Z., Ozga, P. 2020. Electrodeposition of tin-zinc-bismuth alloys from aqueous citrate EDTA baths, *Electrochim. Acta* 338, 135889, <https://doi.org/10.1016/j.electacta.2020.135889>
- [17] Keereeta, Y., Thongtem, T., Thongtem, S. 2014. Effect of medium solvent ratios on morphologies and optical properties of α-ZnMoO₄, β-ZnMoO₄ and ZnMoO₄·0.8H₂O crystals synthesized by microwave-hydrothermal/solvothermal method, *Superlattices and Microstruct.* 69, 253–264, <https://doi.org/10.1016/j.spmi.2014.02.011>
- [18] Keereeta, Y., Thongtem, T., Thongtem, S. 2012. Characterization of

- ZnMoO₄ nanofibers synthesized by electrospinning–calcination combinations, *Mater. Lett.* 68, 265–268, doi:10.1016/j.matlet.2011.10.097
- [19] Kim, H.H., Ogata, S. Oh, A., Futamura, S. 2005. Decomposition of gas-phase benzene using plasma-driven catalyst (PDC) reactor packed with Ag/TiO₂ catalyst, *Appl. Catal. b Environ.* 56, 213–220
- [20] Laohaprapanon, S., Matahum, J., Tayo, L., You, S. 2015. Photodegradation of Reactive Black 5 in a ZnO/Uv slurry membrane reactor, *J. Taiwan. Inst. Chem. Eng.* 49, 136–141, <http://dx.doi.org/10.1016/j.jtice.2014.11.017>
- [21] Liang, Y., Liu, P., Li, H. B., Yang, G. W. 2012. ZnMoO₄ Micro- and Nanostructures Synthesized by Electrochemistry-Assisted Laser Ablation in Liquids and Their Optical Properties, *Cryst. Growth Des.* 12, 4487–4493, dx.doi.org/10.1021/cg3006629
- [22] Liu, X.-R., Sheng, X.-X., Yuan, X.-Y, Liu, J.-K., Sun, X.-W., Yang, X.-H. 2020. Research on correlation between corrosion resistance and photocatalytic activity of molybdenum zinc oxide modified by carbon quantum dots pigments, *Dyes Pigm.* 175, 108148, <https://doi.org/10.1016/j.dyepig.2019.108148>
- [23] Magureanua, M., Mandache, N.B., Parvulescu, V.I. 2015. Degradation of pharmaceutical compounds in water by non-thermal plasma treatment, *Water Res.* 81, 124-136. <http://dx.doi.org/10.1016/j.watres.2015.05.037>
- [24] Mahadwad, O.K., Parikh, P.A., Jasra, R.V., Patil, C. 2011. Photocatalytic degradation of reactive black-5 dye using TiO₂ impregnated ZSM-5, *Bull. Mater. Sci.* 34, 551–556. <https://doi.org/10.1007/s12034-011-0124-2>

- [25] Mahmood, H., Habib, A., Mujahid, M., Tanveer, M., Javed, S., Jamil, A. 2014. Band gap reduction of titania thin films using graphene nanosheets, *Mater. Sci. Semicond. Process.* 24, 193–199.
<http://dx.doi.org/10.1016/j.mssp.2014.03.038>
- [26] Mahmoodi, N.M., Abdi, J., Oveisi, M., Asli, M.A., Vossoughi, M. 2018. Metal-organic framework (MIL-100 (Fe)): Synthesis, detailed photocatalytic dye degradation ability in colored textile wastewater and recycling, *Mater. Res. Bull.*, 100, 357-366,
<https://doi.org/10.1016/j.materresbull.2017.12.033>
- [27] Mei, S., Liu, Y. 2013. Degradation of Reactive Black 5 in Aqueous Solution by Double-Dielectric Barrier Discharge, *Adv. Mat. Res.* 610-613, 1616-1619, <https://doi.org/10.4028/www.scientific.net/AMR.610-613.1616>
- [28] Nijadam S *et al* Sonochemical formation of hydrogen peroxide In: Parvulescu V I, Magureanu M and Lukes P *Plasma Chemistry and Catalysis in Gases and Liquids* New York: Wiley 2012
(DOI:10.1002/9783527649525)
- [29] Oudghiri-Hassani, H., Rakass, S., Abboudi, M., Mohmoud, A., Al Wadaani, F. 2018. Preparation and Characterization of Zinc Molybdate Catalyst: Efficient Sorbent for Methylene Blue and Reduction of 3-Nitrophenol, *Molecules* 23, 1462-16; doi:10.3390/molecules23061462
- [30] Petrović, M., Rančev, S., Prekajski Đorđević, M., Najdanović, S., Velinov, N., Radović Vučić, M., Bojić, A. 2021. Electrochemically synthesized Molybdenum oxides for enhancement of atmospheric pressure non-thermal pulsating corona plasma induced degradation of an organic compound, *Chem. Eng. Sci.* 230, 116209, <https://doi.org/10.1016/j.ces.2020.116209>

- [31] Quintana, A., Varea, A., Guerrero, M., Suriñach, S., Baró, M.D., Sort, J., Pellicer, E. 2015. Structurally and mechanically tunable molybdenum oxide films and patterned submicrometer structures by electrodeposition, *Electrochim. Acta* 173, 705–714
<http://dx.doi.org/10.1016/j.electacta.2015.05.112>
- [32] Rajakumaran, R., Abinaya, M., Chen, S.-M., Balamurugan, K., Muthuraj, V. 2020. Ultrasonication and hydrothermal assisted synthesis of cloud-like zinc molybdate nanospheres for enhanced detection of flutamide, *Ultrason Sonochem* 61, 104823,
<https://doi.org/10.1016/j.ultsonch.2019.104823>
- [33] Ramezani, M., Hosseinpour-Mashkani, M., Sobhani-Nasab, A., Estarki, H.G. 2015. Synthesis, characterization, and morphological control of ZnMoO₄ nanostructures through precipitation method and its photocatalyst application, *J Mater Sci: Mater Electron*, 26, 7588–7594, DOI 10.1007/s10854-015-3395-3.
- [34] Rančev, S., Petrović, M., Radivojević, D., Bojić, A., Maluckov, C., Radović, M. 2019. Prototype of highly efficient liquid electrode pulsating corona plasma reactor for degradation of organics in water, *Plasma Sci. Technol.* 21, 125501
<https://open.ni.ac.rs/handle/123456789/6950>
- [35] Reddy B.J., Vickraman, P., Justin, A.S. 2019. A facile synthesis of novel α -ZnMoO₄ microspheres as electrode material for supercapacitor applications, *Bull. Mater. Sci.* 42:52, <https://doi.org/10.1007/s12034-019-1749-9>
- [36] Ruma, H. Hosano, T. Sakugawa, H. Akiyama. 2018. The Role of Pulse

Voltage Amplitude on Chemical Processes Induced by Streamer Discharge at Water Surface. *Catalysts* 8, 213 – 224.

<https://doi.org/10.3390/catal8050213>

- [37] Sato, M., Tokutake, T., Ohshima, T., Sugiarto, A.T. 2008. Aqueous Phenol Decomposition by Pulsed Discharges on the Water Surface, *IEEE T Ind Appl.* 44, 1397-1402. doi: 10.1109/TIA.2008.2002210
- [38] Shahri, Z., Bazarganipour, M., Salavati-Niasari, M. 2013. Controllable synthesis of novel zinc molybdate rod-like nanostructures via simple surfactant-free precipitation route, *Superlattices Microstruct.* 63, 258–266, <http://dx.doi.org/10.1016/j.spmi.2013.08.020>
- [39] Sun, B., Aye, N.N., Gao, Z., Ly, D., Zhu, X., Sato, M. 2012. Characteristics of gas-liquid pulsed discharge plasma reactor and dye decolouration efficiency, *J. Environ. Sci.* 24, 840 – 845. [https://doi.org/10.1016/S1001-0742\(11\)60837-1](https://doi.org/10.1016/S1001-0742(11)60837-1)
- [40] Wang, D., Huang, M., Zhuang, Y., Jia, H., Sun, J., Guan, M. 2017. Phase- and Morphology-Controlled Synthesis of Zinc Molybdate for Excellent Photocatalytic Property, *Eur. J. Inorg. Chem.* 10.1002/ejic.201701066, <http://dx.doi.org/10.1002/ejic.201701066>
- [41] Wang, L., Wang, J., Lin, J., Zhang, S., Liu, Y. 2018. Degradation of Metronidazole by Radio Frequency Discharge in an Aqueous Solution, *Plasma Process. Polym.* 15, 1700176.
- [42] Zhai, B.-G., Ma, Q.-L., Yang, L., Huang, Y.M. 2017. Growth of ZnMoO₄ nanowires via vapor deposition in air, *Mater. Lett.* 188, 119–122, <http://dx.doi.org/10.1016/j.matlet.2016.11.049>
- [43] Zhang, L., Sun, B., Zhu, X.M. 2009. Organic dye removal from

aqueous solution by pulsed discharge on the pinhole, J. Electrostat. 67, 62 –

66. [DOI: 10.1016/j.elstat.2008.11.003](https://doi.org/10.1016/j.elstat.2008.11.003)